Laser & Photonics Reviews

LASER & PHOTONICS REVIEWS

www.lpr-journal.org

RESEARCH ARTICLE

6G Single-Pixel Meta-Encryption with Ultra-Robustness

Bo Yu[1] | Yifei Xu[1] | Wenwei Liu[1] | Zhancheng Li[1] | Yongliang Liu[1] | Yuanshuo Liu[1] | Qi Liu[1] | Hua Cheng[1] | Shuqi Chen[1,2,3]

[1]The Key Laboratory of Weak Light Nonlinear Photonics, School of Physics and TEDA Institute of Applied Physics, Ministry of Education, Nankai University, Tianjin, China | [2]School of Materials Science and Engineering, Nankai University, Tianjin, China | [3]The Collaborative Innovation Center of Extreme Optics, Shanxi University, Taiyuan, Shanxi, China

Correspondence: Wenwei Liu (wliu@nankai.edu.cn) | Hua Cheng (hcheng@nankai.edu.cn) | Shuqi Chen (schen@nankai.edu.cn)

Received: 6 October 2025 | **Revised:** 22 December 2025 | **Accepted:** 15 January 2026

Keywords: 6G communication | single-pixel encryption | terahertz metasurfaces | ultra-robust transmission

ABSTRACT

As a promising carrier for 6G communication, terahertz waves are particularly susceptible to eavesdropping and transmission sabotage during wireless propagation. However, the existing terahertz encryption schemes are challenging to intrinsically protect the wireless transmission, whose encryption systems are also bulky and hard to integrate. Here, to meet the requirement of confidential 6G wireless links, we propose a single-pixel meta-encryption scheme based on statistical optics empowered Hadamard metasurfaces, which can achieve strong security, key tolerance, and ultra-robustness. The metasurfaces are prepared by 3D printing technology for simple, rapid, and low-cost fabrication. By modulating terahertz waves with Hadamard metasurfaces and combining single-pixel imaging, the scheme achieves a key space size of 10^{90} and 31% key tolerance. Experimental results show that even if 97% of the optical path is severely blocked or there are 30% errors in the key, the transmitted images can be reconstructed. Our approach combines single-pixel imaging with terahertz metasurfaces to address security challenges in future wireless communication, paving the way for secure, robust, and efficient encryption frameworks applicable to communication networks from 6G to XG.

1 | Introduction

The demand for wireless information security and communication speed is continuously growing, driving the future intelligent sixth-generation (6G) communication networks [1]. As a promising solution for 6G wireless communication, terahertz (THz) waves offer ultra-broad bandwidths and terabits-per-second wireless links far beyond microwaves [2]. The unique penetration capability through smoke and dust also makes THz waves more suitable for complex environments compared with optical communication. Traditional encryption schemes based on the complexity of mathematical algorithms are challenged by large-scale computing, such as emerging quantum computing [3], and lack robustness to avoid sabotage. Besides algorithm-based encryption, THz encryption schemes based on physical processes have also been developed, such as using artificial noises for cooperative jamming [4] and physical chaos for signal masking [5]. However, such encryption systems are bulky and hard to integrate, which limits the applications in 6G communication. On the other hand, THz devices for 6G communication, such as sources [6, 7], detectors [8, 9], and beamformers [10, 11], have attracted wide attention from researchers. For example, Zhang et al. reported a 6G meta-device for 3D varifocal projection through rotating each layer to change the focus position [10].

Bo Yu and Yifei Xu contributed equally to this work

Wang et al. presented an on-chip broadband THz topological beamformer using valley vortices for waveguiding, splitting, and isolation [11]. However, for practical applications that are susceptible to eavesdropping and disruption during electromagnetic (EM) waves transmission, how to improve the security and robustness of 6G communication in homogeneous media is an urgent problem to be solved [12, 13]. Both threats pose risks to the confidentiality and facticity of EM signals in wireless propagation.

Meanwhile, metasurfaces, composed of planar arrays of artificial subwavelength structures, that is, optical meta-atoms with remarkable EM responses, open wide possibilities to realize multifunctional EM devices with a compact size. Enabled by abundant local and nonlocal resonances in meta-atoms, metasurfaces could accurately manipulate the amplitude [14, 15], phase [16, 17], and polarization [18, 19] to customize near-field EM modes and thus far-field polarized wavefront [20, 21]. THz metasurfaces have achieved functions for 6G communication, such as signal modulation [22, 23], beam steering [24, 25], and information encryption [26–35]. For example, by employing anisotropic meta-atoms, multi-channel metasurfaces [26, 27] and diffractive neural networks (DNN) [28, 29] can encode EM information into different channels, which can generally be decoded by a correct series of polarization states, thereby limiting the size of key space. Another type of EM encryption is to hide optical information at specific temperatures [30, 31], wavelengths [32], or stretch ratios [33]. Additionally, THz encryption can also be achieved by the metasurface-based logic-gate operation between the plaintext and the key sequence [34, 35]. These schemes suffering from limited key space can possibly be decoded by large amounts of computing attempts.

Apart from security concerns, 6G transmission may also encounter problems such as environmental interference and intentional disruption [36]. For example, EM signals may be accidentally blocked during transmission, or interference may occur when meeting other signals at the same frequency. Improving wireless robustness is crucial to overcome the potential obstacle in the transmission path [37]. Valley photonic crystals have been utilized to avoid on-chip THz scattering based on topological effects [38], but the THz waves coupled to free space still lack intrinsic protection for transmission. Single-pixel imaging (SPI) is a robust computational imaging technology, through single-pixel detection and correlative computation, to realize imaging and extended encryption functionalities [39–41]. Due to precise modulation of optical fields and multiplexing techniques, metasurfaces have emerged as an important platform for single-pixel imaging [42–44]. To meet the demand for future confidential 6G devices, such as strong security, key tolerance, and robustness against obstacles, we propose a single-pixel meta-encryption scheme combining 3D-printed THz Hadamard metasurfaces (HMS) with SPI to encrypt images, instead of complex arrayed sensors with high costs in the THz band. The SPI encryption provides security with the key space size of 10^{90}, 31% key tolerance, and ultra-robustness against sabotage in THz signal transmission. These synergies make our proposed single-pixel meta-encryption scheme a promising solution for securing wireless communication networks and upcoming global intelligent connections.

2 | Principle of the Proposed Meta-Encryption

The proposed 6G single-pixel encryption is based on HMS and SPI through THz single-pixel detection in the public channel and a key transmitted in the private channel, as shown in Figure 1. THz waves carry the information of an arbitrary image with a spatial electric field distribution of $O(x,y)$, which is modulated by a series of HMS for 2^n times with a predefined order. HMS can be considered as linearly independent spatial masks with transmitted complex amplitudes satisfying $\langle \tilde{t}_i(x,y)|\tilde{t}_j(x,y)\rangle = \delta_{ij}$, where δ_{ij} is the Kronecker delta function. A single-pixel detector, irrespective of the spatial resolution, collects focused THz waves as the integration of optical fields $s_i = \iint O(x,y)\tilde{t}_i(x,y)dxdy$. As a result, the ensemble measurement could be expressed as $S = O_r \cdot \Phi$, where S is a row vector consisting of measurements under the order, O_r is a row vector flattened from $O(x,y)$, and Φ is a matrix consisting of row vectors flattened from $\{\tilde{t}_i(x,y)\}_{K_n}$. Due to linear independence of Φ, there must be a matrix Φ^{-1} to reconstruct O through calculating O_r by Equation (1):

$$O_r = O_r \cdot \Phi \cdot \Phi^{-1} = S \cdot \Phi^{-1} \tag{1}$$

Thus, one can reconstruct the original image through the single-pixel measurement from a public channel and the randomly ordered key from a private channel. As shown in Figure 2a, the spatial phase distributions of HMS are 2^n coded matrices ($2^{n/2} \times 2^{n/2}$) with linear independence consisting of phase 0 (white) and π (black), which are split from the 2^n Hadamard matrix row by row. These matrices are ordered and coded by rows and columns, such as A5E2B1…, and the random order is defined as the key. The detailed encryption scheme is shown in Figure 2b, where exists a sender *Alice*, a receiver *Bob*, an eavesdropper *Eve*, and a saboteur *Mallory*. The plaintext from *Alice* is encoded by the HMS to the ciphertext transmitted in the public channel, and the key is transmitted in the private channel. During the THz wireless signals transmitting in the public channel, *Eve* would eavesdrop and decrypt through large amounts of computing attempts; *Mallory* would sabotage THz wireless signals, where we recognize an obstacle in the transmission path as a typical kind of sabotage.

On one hand, *Eve* cannot obtain the plaintext without the key, even though large amounts of computing attempts are employed, because the key space, that is, the set of all possible keys, exceeds the decryption capability of computers. The size of the key space is defined as the amount of all potential keys. The coded matrices are used to encrypt plaintext with a random order, generating the key space. For example, the order A5E2B1…B3H7 serves as one of the keys. Thus, we obtain the key space size of $2^n!$ due to the full permutation of matrices in Figure 2a. The key length is $k = 2^n = 64$ for $n = 6$, and the key space size is KSS $= 2^n!$ with 90 orders of magnitude, which is large enough to guarantee security as shown in Figure 1.

Moreover, key tolerance indicates that users could correctly decode the carried information even with a partly wrong key. As shown in Figure 2c, although the key tolerance may also lead to a reduction in security, the overall security remains sufficient when the key space is large enough. When the accuracy rate of the key is 69% (among the 64-character key, 44 characters appear

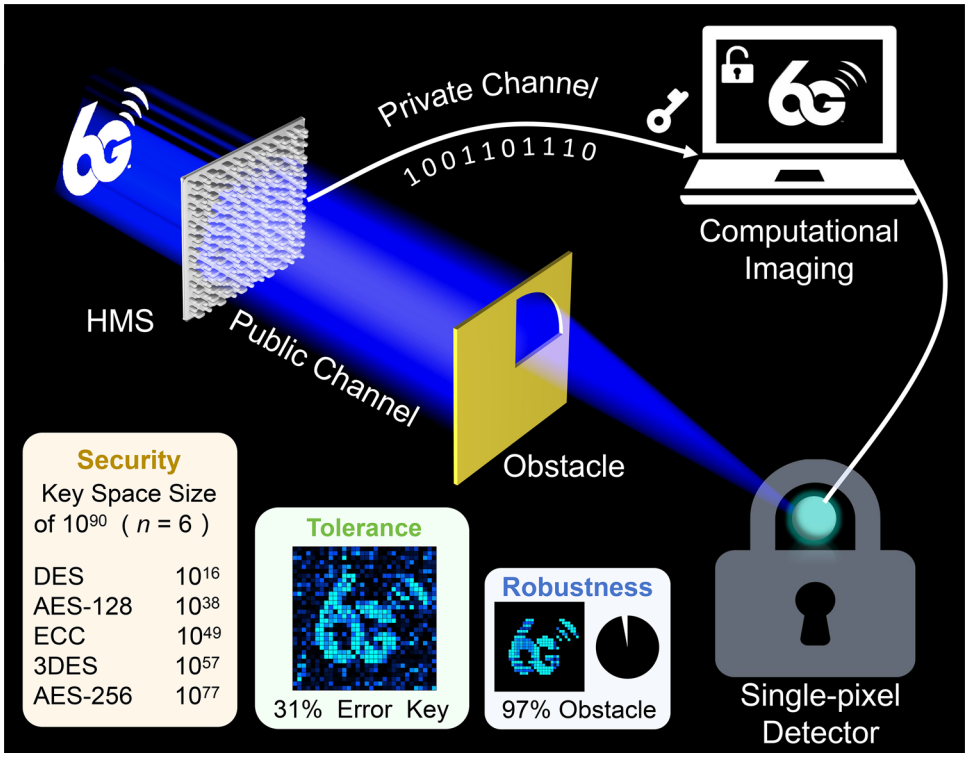

FIGURE 1 | Schematic of the proposed single-pixel meta-encryption. The proposed 6G single-pixel encryption scheme is based on HMS and computational imaging through THz single-pixel sequence detected in a public channel and a key transmitted in a private channel. The inset illustrates the security comparing the KSS with other encryption algorithms [45], the tolerance with 31% error key, and the robust image-reconstruction with 97% obstacle.

in the correct position), the expectation of brute-force decoding according to Poisson distribution relation can be calculated as $E(44) = 1/\sum_{i=44}^{64}\left\{(64-i)! \times \sum_{j=0}^{64-i}\left[\frac{(-1)^j}{j!}\right] \times \left(\frac{1}{i!}\right)\right\}$, reaching 10^{55}. The error rate of images is defined by $r_{error} = 1 - \rho_{O,R} = 1 - \frac{cov(O,R)}{\sigma_O \sigma_R}$ to compare the difference between the origin image and the reconstructed image, where $\rho_{O,R}$ is the Pearson correlation coefficient, O is the origin image, R is the reconstructed image, σ_O/σ_R is the standard deviation of O/R, and $cov(O,R)$ is their covariance. In this case, the reconstructed image "N" is just recognizable ($r_{error} = 50\%$) with the key tolerance of 31%. A Pearson correlation coefficient between 0.3 and 0.7 is considered as moderate positive linear correlation in statistics. Here, we define 50% error rate of images as the threshold for recognizable reconstruction.

The proposed SPI encryption scheme is compared with the Advanced Encryption Standard (AES) encryption scheme, one of the most widely used standard encryption algorithms, in terms of key entropy (KE) and brute-force resistance (BR). The KE is defined by $KE = \log_2(KSS)$, and the BR is defined as the expectation of brute-force decoding. Figure 2d shows that the KE of AES schemes is much smaller than that of the SPI scheme under the same k, and the difference increases as k grows. Similarly, the ratio of their BR indicates that SPI exhibits superior BR. Therefore, compared with AES encryption schemes, our proposed SPI encryption scheme based on the full permutation key has stronger security. And compared with other encryption algorithms in the inset of Figure 1, the key space of the proposed single-pixel meta-encryption also performs well [45]. Therefore, the proposed meta-encryption provides 31% key tolerance in the 64-character key while maintaining enough security.

On the other hand, *Bob* can obtain the plaintext decoded by the key, even after *Mallory*'s sabotage with a large-area obstacle in the optical path. When the optical path is partially obscured during the transmission of THz waves, the plaintext could still be recovered [46]. As shown in Figure 2e, we simulated the computational image "N" at different obstacle rates (defined by the angle of obscured area normalized by 2π) during transmission, where the original image could be numerically reconstructed with the obstacle rate up to 97%. The THz waves gradually become uniformly distributed as the propagation distance increases due to diffraction and transmission, meaning that each spatial point contains abundant momentum components of the original image. The spatial optical field carrying the plaintext also diffuses over the entire plane as the distance increases. Although only a part of the optical field is collected, the global optical information is also obtained. Then we utilize the angular spectrum method to calculate the electric fields evolution from the HMS plane to the obstacle plane in Figure 2f, where we define the distance between the two planes as z. The electric fields on the HMS plane could be transformed to the angular spectrum under the paraxial approximation by Equation (2):

$$A_1(k_x, k_y) = \iint E_1(x_1, y_1) e^{-i(k_x x_1 + k_y y_1)} dx_1 dy_1 \qquad (2)$$

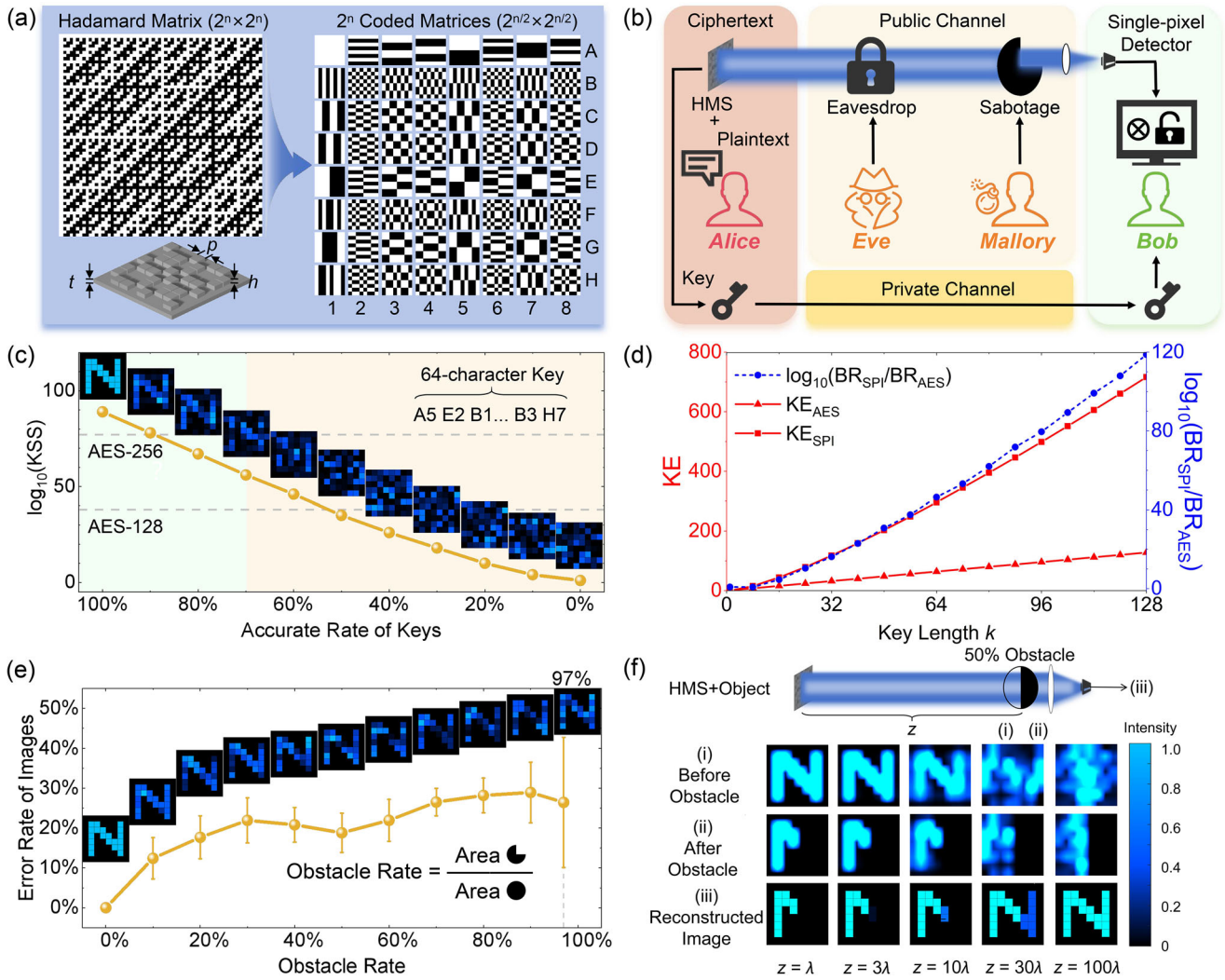

FIGURE 2 | Principle of single-pixel meta-encryption. (a) The Hadamard matrix is split by rows into encoded matrix groups as the phase distribution of metasurfaces. (b) The detailed encryption scheme with a sender *Alice*, a receiver *Bob*, an eavesdropper *Eve*, and a saboteur *Mallory*. (c) Calculated relation between the security quantified by KSS and the tolerance quantified by the accurate rate of keys. (d) Comparison with AES schemes in terms of key entropy and brute-force resistance. (e) Ultra-robustness quantified by the error rate of images at different obstacle rates. (f) Calculated evolution of intensity distribution and reconstructed images with propagation distance z.

where $E_1(x_1,y_1)$ is the electric field on the HMS plane, and $k_x/k_y/k_z$ are wave vectors in $x/y/z$ directions. The electric fields after the transmitted distance z could be expressed by Equation (3):

$$E_2(x_2,y_2) = \frac{1}{(2\pi)^2}\iint A_1(k_x,k_y)e^{ik_z z}e^{i(k_x x_2+k_y y_2)}dk_x dk_y \quad (3)$$

The THz waves transmitting through the obstacle plane with an obstacle function of $\tau(x_2,y_2)$ are focused onto a single point for reconstruction, which could be expressed by Equation (4):

$$s_i = \iint \tau(x_2,y_2)E_2(x_2,y_2)dx_2dy_2 \quad (4)$$

During the calculation of the angular spectrum method, we could find that when the distance z increases, the transmitted spatial distribution tends toward uniformity owing to diffraction during the beam propagation, as shown in Figure 2f. As a result, the obstacle imposes an approximate effect for each measurement in the single-pixel imaging, and the influence of $\tau(x_2,y_2)$ could be minimized while maintaining the ensemble detection. As shown in Figure 2f, the contrast of the electrical intensity before the obstacle decreases as the propagation distance z increases, and the obstacle can be overcome when the distance z is large enough. For example, for $z > 0.1$ m at 0.3 THz, the influence of obstacles on the reconstructed image can be ignored, and the obstacle can be overcome. As shown in Figure 2e, even when the obstacle rate reaches 97%, the original image can still be reconstructed with an average error rate of 26%. It is worth noting that modulated THz waves with millimeter wavelengths at least require a decimeter-scale distance z to achieve the ultra-robustness, which is easily realizable for real-world wireless communication applications.

3 | Experimental Demonstration

To verify the 6G single-pixel meta-encryption scheme, a terahertz time-domain spectroscopy (THz-TDS) system was built to con-

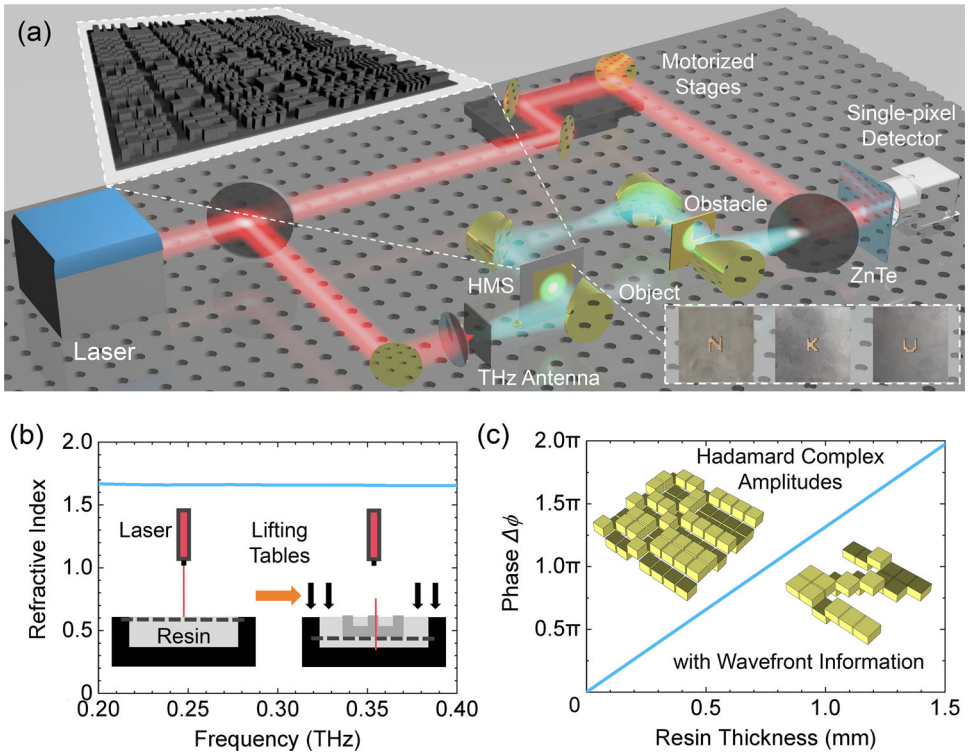

FIGURE 3 | Experimental setup and sample preparation. (a) Schematic of the HMS sample, the object to be transmitted, the obstacle, and the THz-TDS system, consisting of a laser, a THz antenna, a ZnTe crystal, motorized stages, and a single-pixel detector. (b) Refractive index of photosensitive resin and Stereo Lithography Appearance (SLA) process. (c) The relation of resin thickness and phase at 0.3THz, and the insets show the Hadamard complex amplitude before and after loading the wavefront information.

duct single-pixel imaging experiments, as shown in Figure 3a. A 780 nm beam from a femtosecond laser passes through a semi-transparent and semi-reflective mirror (STRM), divided into a pump beam and a detecting beam. A THz antenna is illuminated by the pump light to generate THz waves, which are collimated through an off-axis parabolic (OAP) reflector. Collimated THz waves illuminate a target object carrying the original image and a closely aligned HMS. The original image is encrypted by moving the HMS to switch different phase matrices. The single-pixel detector records the complex amplitude of THz waves for each measurement and finally forms a single-pixel sequence. We employed here a translation stage to control the sequence. Note that the limitation of the mechanical translation is not fundamental. One can use reconfigurable metasurfaces based on *n*-doped GaAs [47], liquid crystal [48], or graphene [49], to speed up the performance with the pivotal properties of our scheme maintained. A metal obstacle is placed in the optical path before THz waves are focused by OAP onto a ZnTe crystal. The detecting beam after the time-delay also illuminates onto the crystal to realize coherent measurement of the THz waves. At last, the THz signals are obtained by the single-pixel detector. Through correlation calculation between the measured sequence and the key, images are reconstructed.

The HMS sample was fabricated by 3D printing technology based on Stereo Lithography Appearance (SLA) with photosensitive resin, as shown in the inset of Figure 3b. A laser cured the resin point by point, and the structure was stacked layer by layer through moving the lifting table. Compared with the typical semiconductor-based processes, 3D printing based on SLA is advantageous in aspects such as speed, cost, and procedure for fabricating the structures responding to the THz wavelength. As shown in Figure 3b, we measured the refractive index of a layer of photosensitive resin obtained through 3D printing. According to the relation between the refractive index and phase difference in Figure 3c, we could choose the required resin thickness of the meta-atoms. The insets show the Hadamard complex amplitude distribution before and after loading the wavefront information in HMS. The 3D printing technology simplifies the fabrication process of HMS, and the single-pixel detection avoids complex array sensors at high costs in the THz band.

The experimental results of single-pixel imaging are shown in Figure 4, where the images of "N", "K", and "U" are reconstructed by the single-pixel sequence and the key. Figure 4a–d show the experimental results at different obstacle rates of 0% (without obstacle), 50%, 88%, and 97%, which could be recognized as "N", "K", and "U". It could be found that the images can be reconstructed even if the obstacle rate reaches 97%, which means most of the optical distribution is recklessly obstructed during optical transmission, verifying the ultra-robustness of the proposed 6G single-pixel meta-encryption. Compared with the simulation results in Figure 2d, the experiment results contain some errors, especially at a high obstacle rate. Such errors are possibly caused by imperfections of optical path alignment, fabrication, and random noises of the THz-TDS system, whose influence is quantified by the signal-to-noise ratio (SNR) is discussed in the next section. Among them, the SNR at various obstacle rates is 22.47 dB without obstacle, 18.43 dB with 50%

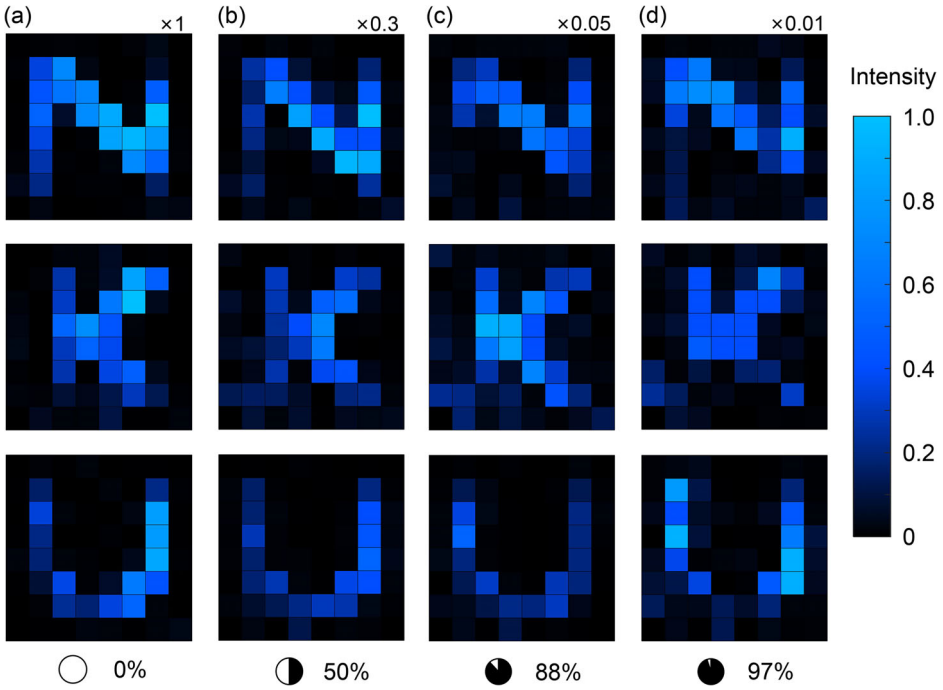

FIGURE 4 | Experimental results at different obstacle rates. The measured target images of "N", "K", and "U" with single-pixel imaging at different obstacle rates of (a) 0%, (b) 50%, (c) 88%, and (d) 97%.

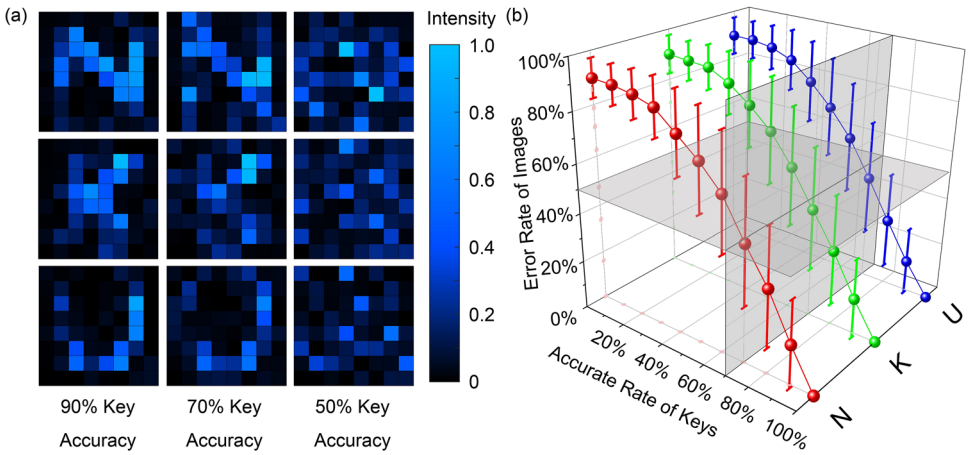

FIGURE 5 | Experimental results decoded by the keys with different accurate rates. (a) Images of "N", "K", and "U" were decoded by 90%, 70%, and 50% accurate keys. (b) The relations between the accurate rate of keys and the error rate of images.

obstacle, 13.30 dB with 88% obstacle, and 8.20 dB with 97% obstacle, respectively.

We also demonstrate the keys with different accurate rates to decode the measured intensity, as shown in Figure 5. It could be found that the keys with 90% and 70% accurate rates are sufficient to reconstruct "N", "K", and "U", while the images decoded by the keys with a 50% accurate rate are unrecognizable. We calculated the errors of the experimentally reconstructed images compared with the original images for various accurate rates of keys in Figure 5b. As a result, the error rate of the reconstructed images gradually approaches about 90%, that is, unrecognizable reconstruction, with the accuracy rate of keys decreasing from 100% to 0%. The horizontal cross-section in Figure 5b represents the threshold for recognizable reconstruction with the 50% error rate of images. It can be observed that the three points obtained at 70% key accuracy are located near this cross-section, which verifies the key tolerance. The experimental results are consistent with the theoretical results. Their difference is caused by environmental noise and other experimental factors. It also means that the eavesdropper *Eve* has to steal at least 70% key to adequately recover the original EM information. These results demonstrate that the proposed meta-encryption scheme provides a balance between key tolerance and strong security.

4 | Discussion

In real applications, the SNR determined by the system and the environment is critical to the performance and the quality of

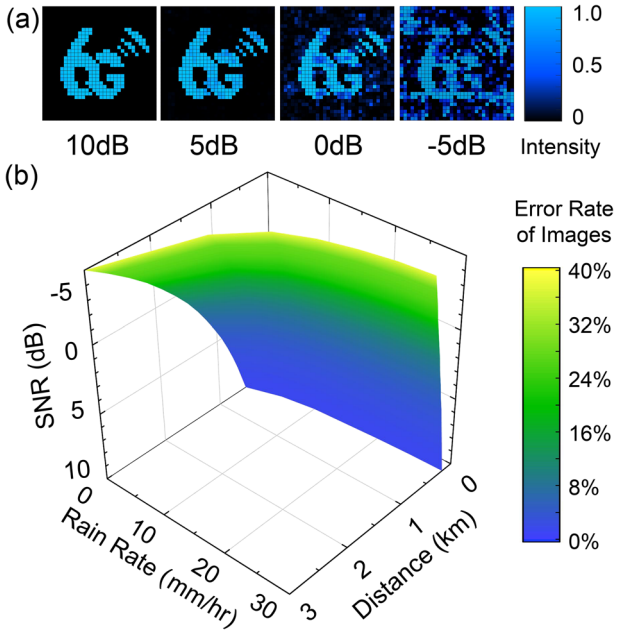

FIGURE 6 | SNR influence to 6G single-pixel meta-encryption. (a) The constructed images of "6G" with various SNR from −5 to 10 dB. (b) The relation among SNR, the rain rate, transmission distances, and the error rate of images.

wireless communication. We calculated the SNR influence on the 6G single-pixel meta-encryption scheme, as shown in Figure 6. The target image is a 32 × 32-pixel logo of 6G communication approved by third Generation Partnership Project (3GPP). The reconstructed results are demonstrated with SNR from 10 to −5 dB in Figure 6a, where the image with 0 dB SNR (noise is comparable to signal) is still recognizable, and SNR = −5 dB is the recognition limit. Generally, the transmission distance and the air humidity are the most important parameters to determine SNR for a given THz system. According to the data in Ref. [50, 51], we calculated the relation between the image quality (defined by the error rate of images) and the environment (characterized by the transmission distance and the rain rate) for various SNR. It could be found that even with the −5 dB condition of 3 km distance on a sunny day or 0.5 km under a 30 mm/hr rain rate, the image can be well-reconstructed with 40% error rate of images, which is under the recognition boundary about 50% in Figure 5b.

The proposed metasurface offers ultra-robust reconstruction during single-pixel encryption. The reconstructed images hold the ultra-robustness originating from statistical optics under various types of disturbances (31% key fault, 97% obstacle during light transmission, and −5 dB SNR) through the Hadamard metasurfaces coding and the single-pixel detection. We summarize representative studies on THz encryption in Table 1 in terms of key space, key tolerance, robustness, fabrication, and detection. Compared with existing THz meta-encryption approaches [26–35], our proposed easy-fabricating single-pixel meta-encryption scheme excels in key space, key tolerance, and transmission robustness. (1) Compared with the key-space size in the independent combination schemes (exponential functions such as 2^k, 4^k or 8^k), the key-space size in the full permutation scheme of our work (factorial function of $k!$) provides the larger key-space enhancing the security for larger k values, where k is the key length. (2) The key tolerance of conventional encryption schemes is based on the following principle: a specific range of the operational temperature [30, 31] or tensile force [33] applied on the metasurfaces can serve as the key, and our proposed single-pixel encryption scheme can tolerate a key with arbitrary 31% errors. (3) Since there is no unified definition for robustness (e.g., robustness against fabrication errors [28], incident angles [29], and low SNR [35]), we consider the presence or absence of robustness comparison in Table 1. Our scheme focuses on the robustness overcoming obstacles in the transmission path, which is crucial for wireless communications. (4) Compared with the photolithography processes (usually several days and hundreds to thousands of dollars), 3D printing is simpler (direct molding), faster (few hours), and cheaper (several dollars). (5) The single-pixel detection technique is especially suitable for the THz band to avoid complex and expensive THz arrayed sensors. We also do not need scanning of the signal compared with the probe scanning method.

Our single-pixel meta-encryption scheme is a proof-of-concept framework, and there is a certain distance from practical applications, primarily limited by the mechanical scanning speed. Our encryption scheme could be feasibly realized in the THz programmable metasurfaces (such as using dynamic materials GaAs, liquid crystal, or graphene), which have been reported in THz single-pixel imaging [47–49]. In an encryption scenario, the sender utilizes programmable metasurfaces with our key-coding method to modulate the spatial THz fields, achieving real-time and high-speed encryption. And the receiver decodes the signal from single-pixel detection with the key to obtain encrypted images. We believe this scheme provides a valuable approach for the security and robustness of future 6G communication. Moreover, the single-pixel meta-encryption scheme can be further improved with data-driven deep learning algorithms to reduce the required amount of data and enhance the quality of the images [52, 53]. Our scheme can also be applied in massive multiple-input multiple-output (MIMO) systems [54, 55], frequency division multiplexing (FDM) systems [56, 57], or multiplexing SPI metasurfaces [41, 42] to increase the data-transmission capacity.

5 | Conclusions

In conclusion, a single-pixel meta-encryption framework for 6G communication devices is proposed, which features strong security with the KSS of 10^{90}, 31% key tolerance, and ultra-robustness against obstacles. The THz waves carrying an image are modulated by HMS and collected by a single-pixel detector in the public channel. The private key is transmitted in the private channel. The strong security and the ultra-robustness can avoid eavesdropping, decryption, and transmission sabotage, respectively. HMS are fabricated by 3D printing technology for simple, rapid, and low-cost fabrication. A THz-TDS system is built for SPI to avoid complex array sensors with high costs in the THz band. The experimental results verify that the original images can be reconstructed even with a 97% obstacle during transmission or a 30% wrong key. In addition, the SNR influence has been discussed that the target image can be recognized with −5 dB SNR, which enables the transmission over long distances and in high humidity. Compared with other THz encryption schemes,

TABLE 1 | Comparison among representative works of THz meta-encryption.

Ref.	Encryption Scheme	Key Space	Key Tolerance	Robustness	Fabrication	Detection
26	Coding information into Stokes parameters	4^k	×	—	Photolithography	Probe Scanning
27	Hiding information in polarization channels	8^k	—	—	UV Photolithography	Focal-plane Imaging
28	Permutation operation by DNN	8^k	—	√	3D Printing	Detector Scanning
29	Coding information into polarized states in DNN	8^k	×	√	—	Probe Scanning
30	Hiding information in temperature and direction channels	4^k	√	—	UV Photolithography	Nonlinear Imaging
31	Hiding information in a temperature channel	2^k	√	—	Photolithography	Probe Scanning
32	Hiding information in a wavelength channel	—	—	—	UV Photolithography	—
33	Hiding information in a stretched state channel	—	√	—	Kirigami	Spectrum Measuring
34	Logic operation with a temporal voltage signal	2^k	×	—	Photolithography	Single-pixel Detecting
35	Logic operation with a temporal near-infrared signal	2^k	×	√	E-beam lithography	Integrated Detecting
This Work	**Single-pixel imaging**	***k*!**	√	√	**3D Printing**	**Single-pixel Detecting**

our proposed scheme performs well in the aspects of security, tolerance, robustness, and simplicity. Our approach paves the way for future high-performance wireless communication and remote sensing from 6G to XG.

Funding

This work was supported by the National Key Research and Development Program of China (2021YFA1400601 and 2024YFA1409903), the National Natural Science Foundation of China (W2441005, 12192253, 11274239, 12274237, 12474331, and U22A20258).

Conflicts of Interest

The authors declare no conflicts of interest.

Data Availability Statement

The data that support the findings of this study are available from the corresponding author upon reasonable request.

References

1. S. Dang, O. Amin, B. Shihada, and M.-S. Alouini, "What Should 6G be?," *Nature Electronics* 3 (2020): 20–29, https://doi.org/10.1038/s41928-019-0355-6.

2. H. Chen, H. Sarieddeen, T. Ballal, H. Wymeersch, M.-S. Alouini, and T. Y. Al-Naffouri, "A Tutorial on Terahertz-Band Localization for 6G Communication Systems," *IEEE Communications Surveys & Tutorials* 24 (2020): 1780–1815, https://doi.org/10.1109/COMST.2022.3178209.

3. H.-S. Zhong, H. Wang, Y.-H. Deng, et al., "Quantum Computational Advantage Using Photons," *Science* 370 (2020): 1460–1463, https://doi.org/10.1126/science.abe8770.

4. L. Zhang, Q. Deng, H. Zhang, et al., "Quantum Noise Secured Terahertz Communications," *IEEE Journal of Selected Topics in Quantum Electronics* 29 (2023): 1–10, https://doi.org/10.1109/JSTQE.2022.3218848.

5. Q. Deng, L. Zhang, Z. Lyu, X. Pang, O. Ozolins, and X. Yu, "Private Communication with Photonic Terahertz Chaos," *Advanced Photonics* 6, no. 6 (2024): 066004, https://doi.org/10.1117/1.AP.6.6.066004.

6. J. Pettine, P. Padmanabhan, T. Shi, et al., "Light-Driven Nanoscale Vectorial Currents," *Nature* 626 (2024): 984–989, https://doi.org/10.1038/s41586-024-07037-4.

7. S. Han, Y. Chua, Y. Zeng, et al., "Photonic Majorana Quantum Cascade Laser with Polarization-Winding Emission," *Nature Communications* 14 (2023): 707, https://doi.org/10.1038/s41467-023-36418-y.

8. J. Shi, D. Yoo, F. Vidal-Codina, et al., "A Room-Temperature Polarization-Sensitive CMOS Terahertz Camera Based on Quantum-Dot-Enhanced Terahertz-to-Visible Photon Upconversion," *Nature Nanotechnology* 17 (2022): 1288–1293, https://doi.org/10.1038/s41565-022-01243-9.

9. X. Li, D. Mengu, N. T. Yardimci, et al., "Plasmonic Photoconductive Terahertz Focal-Plane Array with Pixel Super-Resolution," *Nature Photonics* 18 (2024): 139–148, https://doi.org/10.1038/s41566-023-01346-2.

10. J. C. Zhang, G.-B. Wu, M. K. Chen, et al., "A 6G Meta-Device for 3D Varifocal," *Science Advances* 9, no. 4 (2023): adf8478, https://doi.org/10.1126/sciadv.adf8478.

11. W. Wang, Y. J. Tan, T. C. Tan, et al., "On-Chip Topological Beamformer for Multi-Link Terahertz 6G to XG Wireless," *Nature* 632 (2024): 522–527, https://doi.org/10.1038/s41586-024-07759-5.

12. J. Ma, R. Shrestha, J. Adelberg, et al., "Security and Eavesdropping in Terahertz Wireless Links," *Nature* 563 (2018): 89–93, https://doi.org/10.1038/s41586-018-0609-x.

13. J. M. Jornet, E. W. Knightly, and D. M. Mittleman, "Wireless Communications Sensing and Security above 100 GHz," *Nature Communications* 14 (2023): 841, https://doi.org/10.1038/s41467-023-36621-x.

14. R. Chai, W. Liu, Z. Li, et al., "Spatial Information Lasing Enabled by Full-k-Space Bound States in the Continuum," *Physical Review Letters* 132 (2024): 183801, https://doi.org/10.1103/PhysRevLett.132.183801.

15. Y. Liu, W. Liu, Q. Liu, et al., "Dual-Polarized Transmissive Metasurfaces for Near-Unitary-NA Analog Spatial Computing Empowered by Impedance Matching and Mismatching," *Optics Letters* 49 (2024): 4926–4929, https://doi.org/10.1364/OL.536788.

16. W. Liu, D. Ma, Z. Li, et al., "Aberration-Corrected Three-Dimensional Positioning with a Single-Shot Metalens Array," *Optica* 7 (2020): 1706–1713, https://doi.org/10.1364/OPTICA.406039.

17. L. Liu, W. Liu, F. Wang, et al., "Spatial Coherence Manipulationon the Disorder-Engineered Statistical Photonic Platform," *Nano Letters* 22 (2022): 6342–6349, https://doi.org/10.1021/acs.nanolett.2c02115.

18. J. Cheng, Z. Li, D.-Y. Choi, et al., "Counterintuitive Reversal of Circular Dichroism via Controllable Plasmonic Guided Mode Resonance in Diatomic Metasurfaces," *Laser & Photonics Reviews* 19, no. 8 (2025): 2401184, https://doi.org/10.1002/lpor.202401184.

19. Z. Li, S. Yu, G. Geng, et al., "Chiral Guided Mode Resonance with Independently Controllable Quality Factorand Circular Dichroism," *Nano Letters* 25 (2025): 2519–2527, https://doi.org/10.1021/acs.nanolett.4c06157.

20. S. Chen, Z. Li, W. Liu, H. Cheng, and J. Tian, "From Single-Dimensional to Multidimensional Manipulation of Optical Waves with Metasurfaces," *Advanced Materials* 31 (2019): 1802458, https://doi.org/10.1002/adma.201802458.

21. S. Chen, W. Liu, Z. Li, H. Cheng, and J. Tian, "Metasurface-Empowered Optical Multiplexing and Multifunction," *Advanced Materials* 32 (2020): 1805921, https://doi.org/10.1002/adma.201805912.

22. W. He, X. Cheng, S. Hu, et al., "Color Coded Metadevices toward Programmed Terahertz Switching," *Light: Science & Applications* 13 (2024): 142, https://doi.org/10.1038/s41377-024-01495-1.

23. Y. K. Srivastava, M. Manjappa, L. Cong, et al., "A Superconducting Dual-Channel Photonic Switch," *Advanced Materials* 30, no. 29 (2018): 1801257, https://doi.org/10.1002/adma.201801257.

24. W. Li, B. Chen, X. Hu, et al., "Modulo-Addition Operation Enables Terahertz Programmable Metasurface for High-Resolution Two-Dimensional Beam Steering," *Science Advances* 9, no. 42 (2023): adi7565, https://doi.org/10.1126/sciadv.adi7565.

25. D. Shen, F. Lan, L. Wang, et al., "Sub-terahertz Transmissive Reconfigurable Intelligent Surface for Integrated Beam Steering and Self-OOK-modulation," *Light: Science & Applications* 14 (2025): 13, https://doi.org/10.1038/s41377-024-01690-0.

26. T. Wu, Q. Xu, X. Zhang, et al., "Spin-Decoupled Interference Metasurfaces for Complete Complex-Vectorial-Field Control and Five-Channel Imaging," *Advanced Science* 9, no. 35 (2025): 2204664, https://doi.org/10.1002/advs.202204664.

27. H. Zhao, X. Wang, S. Liu, and Y. Zhang, "Highly Efficient Vectorial Field Manipulation Using a Transmitted Tri-layer Metasurface in the Terahertz Band," *Opto-Electronic Advances* 6 (2023): 220012, https://doi.org/10.29026/oea.2023.220012.

28. G. Ma, X. Yang, B. Bai, et al., "Multiplexed all-Optical Permutation Operations Using a Reconfigurable Diffractive Optical Network," *Laser & Photonics Reviews* 18 (2024): 2400238, https://doi.org/10.1002/lpor.202400238.

29. Z. Guo, Z. Tan, X. Zang, et al., "Polarization-selective Unidirectional and Bidirectional Diffractive Neural Networks for Information Security and Sharing," *Nature Communications* 16 (2025): 4492, https://doi.org/10.1038/s41467-025-59763-6.

30. B. Chen, S. Yang, J. Chen, et al., "Directional Terahertz Holography with Thermally Active Janus Metasurface," *Light: Science & Applications* 12 (2023): 136, https://doi.org/10.1038/s41377-023-01177-4.

31. S. Zhu, B. Dong, G. Guo, et al., "Terahertz Metasurfaces for Thermally Controlled Optical Encryption," *Laser & Photonics Reviews* 17 (2023): 2300233, https://doi.org/10.1002/lpor.202300233.

32. H. Zhou, S. Zhang, S. Wang, et al., "Optically Controlled Dielectric Metasurfaces for Dynamic Dual-mode Modulation on Terahertz Waves," *Advanced Photonics* 5, no. 2 (2023): 026005, https://doi.org/10.1117/1.AP.5.2.026005.

33. W. J. Choi, S. H. Lee, M. Cha, and N. A. Kotov, "Chiral Kirigami for Bend-Tolerant Reconfigurable Hologram with Continuously Variable Chirality Measures," *Advanced Materials* 36 (2024): 2401131, https://doi.org/10.1002/adma.202401131.

34. H. Zeng, X. Cong, H. Zhang, et al., "Dynamically Logical Modulation for THz Wave Within a Dual Gate–Controlled 2DEG Metasurface," *Science Advances* 10, no. 49 (2024): adr1448, https://doi.org/10.1126/sciadv.adr1448.

35. L. Han, S. Zhang, S. Tian, et al., "Multispectral Integrated Black Arsenene Phototransistors for High-Resolution Imaging and Enhanced Secure Communication," *ACS Nano* 19 (2025): 3740–3751, https://doi.org/10.1021/acsnano.4c14512.

36. R. Shrestha, H. Guerboukha, Z. Fang, E. Knightly, and D. M. Mittleman, "Jamming a Terahertz Wireless Link," *Nature Communications* 13 (2022): 3045, https://doi.org/10.1038/s41467-022-30723-8.

37. L. Liu, W. Liu, F. Wang, et al., "Ultra-Robust Informational Metasurfaces Based on Spatial Coherence Structures Engineering," *Light: Science & Applications* 13 (2024): 131, https://doi.org/10.1038/s41377-024-01485-3.

38. Y. Yang, Y. Yamagami, X. Yu, et al., "Terahertz Topological Photonics for On-Chip Communication," *Nature Photonics* 14 (2020): 446–451, https://doi.org/10.1038/s41566-020-0618-9.

39. M. P. Edgar, G. M. Gibson, and M. J. Padgett, "Principles and Prospects for Single-Pixel Imaging," *Nature Photonics* 13 (2019): 13–20, https://doi.org/10.1038/s41566-018-0300-7.

40. P. Clemente, V. Durán, V. Torres-Company, E. Tajahuerce, and J. Lancis, "Optical Encryption Based on Computational Ghost Imaging," *Optics Letters* 35 (2010): 2391–2393, https://doi.org/10.1364/OL.35.002391.

41. H. Xiong, R. Zhao, C. Tian, et al., "Metasurface-Enabled Dual-Channel Single-Pixel Polarimetric Imaging," *Laser & Photonics Reviews* (2025): e01878, https://doi.org/10.1002/lpor.202501878.

42. J. Yan, Q. Wei, Y. Liu, et al., "Single Pixel Imaging Key for Holographic Encryption Based on Spatial Multiplexing Metasurface," *Small* 18 (2022): 2203197, https://doi.org/10.1002/smll.202203197.

43. H.-C. Liu, B. Yang, Q. Guo, et al., "Single-Pixel Computational Ghost Imaging with Helicity-Dependent Metasurface Hologram," *Science Advances* 3, no. 9 (2017): 1701477, https://doi.org/10.1126/sciadv.1701477.

44. P. Zheng, Q. Dai, Z. Li, et al., "Metasurface-Based Key for Computational Imaging Encryption," *Science Advances* 7, no. 21 (2021): abg0363, https://doi.org/10.1126/sciadv.abg0363.

45. S. Chandra, S. Paira, and S. S. Alam, et al., "A Comparative Survey of Symmetric and Asymmetric Key Cryptography," in 2014 International Conference on Electronics, Communication and Computational Engineering, (2014): 83–93, https://doi.org/10.1109/ICECCE.2014.7086640.

46. C. Gao, X. Wang, L. Gou, et al., "Ghost Imaging for an Occluded Object," *Laser Physics Letters* 16 (2019): 065202, https://doi.org/10.1088/1612-202X/ab0c8d.

47. C. M. Watts, D. Shrekenhamer, J. Montoya, et al., "Terahertz Compressive Imaging with Metamaterial Spatial Light Modulators," *Nature Photonics* 8 (2014): 605–609, https://doi.org/10.1038/nphoton.2014.139.

48. W. Li, X. Hu, J. Wu, et al., "Dual-Color Terahertz Spatial Light Modulator for Single-Pixel Imaging," *Light: Science & Applications* 11 (2022): 191, https://doi.org/10.1038/s41377-022-00879-5.

49. Y. Malevich, M. S. Ergoktas, G. Bakan, P. Steiner, and C. Kocabas, "Very-Large-Scale Reconfigurable Intelligent Surfaces for Dynamic Control of Terahertz and Millimeter Waves," *Nature Communications* 16 (2025): 2907, https://doi.org/10.1038/s41467-025-58256-w.

50. K. Liu, Y. Feng, C. Han, et al., "High-Speed 0.22 THz Communication System with 84 Gbps for Real-Time Uncompressed 8K Video Transmission of Live Events," *Nature Communications* 15 (2024): 8037, https://doi.org/10.1038/s41467-024-52370-x.

51. Y. Song, J. Cui, G. Liu, et al., "Terahertz Channel Power and BER Performance in Rain," *Optics Express* 33 (2025): 11336–11349, https://doi.org/10.1364/OE.551220.

52. H. Wang, L. Bian, and J. Zhang, "Depth Acquisition in Single-Pixel Imaging with Multiplexed Illumination," *Optics Express* 29, no. 4 (2021): 4866–4874, https://doi.org/10.1364/OE.416481.

53. Y. He, G. Wang, G. Dong, et al., "Ghost Imaging Based on Deep Learning," *Scientific Reports* 8 (2018): 6469, https://doi.org/10.1038/s41598-018-24731-2.

54. Z. Wan, Z. Gao, F. Gao, M. D. Renzo, and M.-S. Alouini, "Terahertz Massive MIMO with Holographic Reconfigurable Intelligent Surfaces," *IEEE Transactions on Communications* 69 (2021): 4732–4750, https://doi.org/10.1109/TCOMM.2021.3064949.

55. M. Cui, Z. Wu, Y. Lu, X. Wei, and L. Dai, "Near-Field MIMO Communications for 6G: Fundamentals, Challenges, Potentials, and Future Directions," *IEEE Communications Magazine* 61 (2023): 40–46, https://doi.org/10.1109/MCOM.004.2200136.

56. N. J. Karl, R. W. McKinney, Y. Monnai, R. Mendis, and D. M. Mittleman, "Frequency-Division Multiplexing in the Terahertz Range Using a Leaky-Wave Antenna," *Nature Photonics* 9 (2015): 717–720, https://doi.org/10.1038/nphoton.2015.176.

57. H. Cao, Z. Wang, W. Wang, et al., "8K Real-Time Video-Transmission Using PDM and FDM in 220-GHz Band Based on Polarization Crosstalk Model and Optimization Strategy," *IEEE Communications Magazine* 62 (2019): 86–93, https://doi.org/10.1109/MCOM.001.2400019.